

A Visual Analytics Framework for Reviewing Multivariate Time-Series Data with Dimensionality Reduction

Takanori Fujiwara, Shilpika, Naohisa Sakamoto, Jorji Nonaka, Keiji Yamamoto, and Kwan-Liu Ma

Abstract— Data-driven problem solving in many real-world applications involves analysis of time-dependent multivariate data, for which dimensionality reduction (DR) methods are often used to uncover the intrinsic structure and features of the data. However, DR is usually applied to a subset of data that is either single-time-point multivariate or univariate time-series, resulting in the need to manually examine and correlate the DR results out of different data subsets. When the number of dimensions is large either in terms of the number of time points or attributes, this manual task becomes too tedious and infeasible. In this paper, we present MuTiDR, a new DR framework that enables processing of time-dependent multivariate data as a whole to provide a comprehensive overview of the data. With the framework, we employ DR in two steps. When treating the instances, time points, and attributes of the data as a 3D array, the first DR step reduces the three axes of the array to two, and the second DR step visualizes the data in a lower-dimensional space. In addition, by coupling with a contrastive learning method and interactive visualizations, our framework enhances analysts' ability to interpret DR results. We demonstrate the effectiveness of our framework with four case studies using real-world datasets.

Index Terms— Multivariate time-series, tensor, data cube, dimensionality reduction, interpretability, visual analytics

1 INTRODUCTION

Analysis of multivariate time-series data is becoming increasingly important to studying various phenomena in the real world. For example, analyzing electronic health records (EHRs) that contain temporal changes of individuals' various medical measures (e.g., blood pressure and heart rate) for cohort studies can help clinical researchers develop healthcare plans [24, 27, 33]. Many other analysis examples can be found in other domains, such as diagnosis of the performance of parallel computing systems [22, 23, 40], fault detection of factory assembly lines [57–59], and optimization of transportation systems [15, 35]. As seen in the emergence of the Internet of Things, the growing capability and use of sensing devices improves the granularity, quality, and accessibility of multivariate time-series data [2, 16, 47]; at the same time, the increase of the data size and dimensionality makes analysis tasks more challenging [2].

To effectively analyze and visualize large, high-dimensional data, dimensionality reduction (DR) methods are often used [36, 45] because of their ability to provide a succinct overview of such complex data. Currently available DR methods designed for 2D or 3D visualization [14, 53] can be only applied to data that can be formed into a 2D matrix, such as single-time-point multivariate data (matrix rows: instances, columns: variables), univariate time-series data (rows: instances, columns: time points), and multivariate time-series with a single instance (rows: time points, columns: variables). When multivariate time-series data consists of multiple instances, the data is often represented as a third-order tensor (or 3D array); consequently, we either cannot directly apply some DR methods such as principal component analysis to the data or we do not know how to properly prepare a distance matrix as an input for other DR methods (e.g., t-SNE [52]).

A common approach to the above problem is slicing the 3D array and then applying a DR method to each resulting slice [5]. For instance, when slicing along a temporal direction, where each slice represents a matrix of instances and variables, we can visualize a set of DR results with animation or small multiples [5]. However, when a sliced direction has high dimensionality (e.g., 100 time points), the analyst must examine a large amount of DR results and can easily overlook

important patterns (e.g., the emerge of outliers).

To support effective analysis of multivariate time-series data, we introduce a visual analytics framework, MuTiDR, which employs a two-step DR to generate an overview of the data and supports interpreting the DR results with contrastive learning (CL) and interactive visualization. Particularly, in the first step of DR, MuTiDR compresses and converts a third-order tensor into a matrix, and then, in the second step, it projects high-dimensional data points into a lower-dimensional space. Similar to the existing DR methods, the two-step DR result shows similarities of instances, variables, or time points and enables visual identification of essential patterns, such as clusters and outliers. When compared with ordinary DR, the two-step DR result is derived from two different directions (e.g., variables and time points) and could be more difficult to understand why specific patterns appear. Thus, to support the analysis of the two-step DR, we integrate CL to identify essential aspects for the analysts to review and interpret in detail with interactive visualization. We demonstrate the effectiveness of MuTiDR for multivariate time-series analysis with multiple case studies using real-world datasets and also make qualitative comparisons of MuTiDR with other potential DR methods.

2 BACKGROUND AND RELATED WORK

We provide a brief description of third-order tensors and discuss relevant works.

2.1 Third-Order Tensors

A third-order tensor is a 3D array (note that first- and second-order tensors correspond to vectors and matrices, respectively). Each axis of a tensor is called *mode*. When a third-order tensor represents multivariate time-series data, the three modes correspond to time points, instances (or samples), and variables (or attributes). As the main analysis target, we focus on third-order tensors of multivariate time-series data; however, our framework, MuTiDR, is designed to be able to deal with the other types of third-order tensors.

The notations used in this paper follow the conventions in the literature [32]. We denote scalars, vectors, matrices, and third-order tensors with lowercase (e.g., x), boldface lowercase (e.g., \mathbf{x}), boldface uppercase (e.g., \mathbf{X}), and boldface Euler script (e.g., \mathfrak{X}) letters, respectively. We use indices $t = 1, \dots, T$, $n = 1, \dots, N$, and $d = 1, \dots, D$ for time points, instances, and variables, respectively. Here T , N , and D are lengths of modes of time points, instances, and variables, respectively (i.e., a third-order tensor $\mathfrak{X} \in \mathbb{R}^{T \times N \times D}$).

• Takanori Fujiwara, Shilpika, and Kwan-Liu Ma are with University of California, Davis. E-mail: {tfujiwara,fshilpika,klma}@ucdavis.edu.

• Naohisa Sakamoto is with Kobe University. E-mail: naohisa.sakamoto@people.kobe-u.ac.jp.

• Jorji Nonaka and Keiji Yamamoto are with RIKEN R-CCS. E-mail: {jorji,keiji.yamamoto}@riken.jp.

2.2 Related Work

Our work relates to visual analytics of third-order tensors. A third-order tensor commonly found in the visualization field is a “generalized” space-time cube [4, 5]. A generalized space-time cube represents a 2D visualization space that changes over time (e.g., temporal geospatial visualizations and animated 2D scatterplots). Bach et al. [4, 5] provided a comprehensive survey of visualizations of generalized space-time cubes. They also provided a categorization of visualization strategies. The strategies include 3D rendering (i.e., render a cube as it is), time cutting (i.e., extracting a 2D snapshot at a particular time point), time flattening (i.e., collapsing temporal changes into a single 2D image), time juxtaposing (i.e., arranging multiple 2D snapshots as small multiples), space cutting (i.e., extracting a planar cut in one direction of the 2D space), and among others. One strategy that the survey did not discuss in detail is dimensionality reduction (DR), which can be considered as a special form of flattening. Since our framework, MuTiDR, also employs DR, here we focus on discussing the works using DR to visualize third-order tensors.

Similar to our work, a target application of many of the existing works is visualizing multivariate time-series data. One simple strategy is applying DR to a matrix of instances and variables at each time point and then showing temporal changes with animation or juxtaposition. To support such a visualization, the researchers developed dynamic DR methods that provide coherent node positions between consecutive time points, such as the time-based least square projection [3], Dynamic t-SNE [43], and the enhanced incremental principal component analysis (PCA) [20]. However, finding useful patterns, such as outliers or similar time points, is difficult when relying on animation or juxtaposition.

Another common strategy is applying DR based on a dissimilarity of each time point’s matrix [6, 19, 28, 40, 51, 54]. This strategy generates an overview of the (dis)similarities of time points. For example, Bach et al. [6] computed the dissimilarity of each pair of 2D images at different time points with a certain distance measure, such as a Euclidean distance; then applied multidimensional scaling (MDS) based on their dissimilarities. In the MDS result, a 2D image at each time point is visualized as a dot. To convey the time information, they connected dots of two consecutive time points and colored them according to time. Several researchers also used a similar approach to provide a visual summary of dynamic network data [19, 51, 54]. On the other hand, Jäckle et al. [28] visualized an MDS result in a 1D axis and used another axis to represent time. Since MDS may produce unnecessary rotation in the result, they reduced the rotations by flipping the y-coordinates based on their positions in the previous time point. Muelder et al. [40] also took a similar approach but they used a graph layout algorithm as a DR method instead of MDS. However, all the approaches above have several problems. For example, when two modes in each matrix slice have different types (e.g., instances and variables), the DR result might not capture any useful patterns because each mode is mixed together when computing dissimilarities (refer to Sect. 6 for concrete examples). Also, because each dot in the DR result represents a matrix, it is difficult to identify which instances or variables highly relate to a certain pattern appeared in the DR result (e.g., clusters) and, consequently, the result has low interpretability.

While the visualizations above focus on showing the time points’ similarities, some works are to overview the instance similarities over time. For example, Fujiwara et al. [22] used time-series distance measures, such as dynamic-time warping, to obtain the similarity of each instance’s changes in a variable value across time. Afterward, for each variable, they applied MDS or t-SNE to the computed similarities and then juxtaposed the DR results for different variables. Kesavan et al. [29] extended the same approach for streaming high-dimensional data. In contrast to our framework, these approaches handle only one variable in each DR result.

Recently, visualization researchers have started to use tensor decompositions [32, 37] to analyze or simplify third-order tensors. Two most popular tensor decompositions are canonical decomposition (or CP decomposition) [13, 25] and the Tucker decomposition [48]. CP decomposition expresses a tensor as the sum of a finite number of rank-one tensors (i.e., tensor-to-vector decomposition). On the other hand, the

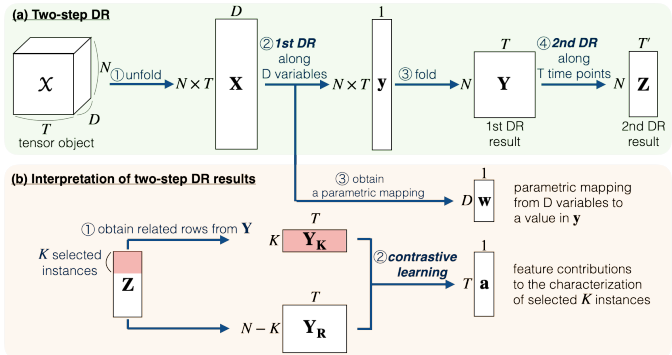


Fig. 1: General architecture of MuTiDR back-end. Here, we demonstrate a case when showing instance similarities based on their temporal changes of variable values.

Tucker decomposition can be considered as a high-order version of PCA and decomposes a tensor to a core tensor and a matrix along each mode (i.e., tensor-to-tensor decomposition). For example, TPFlow [35] introduces a similar method to CP decomposition, which finds the best slice of a space-time cube, where some meaningful patterns likely exist. Voila [12] uses the Tucker decomposition to detect anomalies from a space-time cube. Also, TTHRESH [7] utilizes the Tucker decomposition to compress volume data into a smaller file size. While these works extract important features or elements from third-order tensors, our framework generates an overview from a third-order tensor for visual identification of patterns, such as clusters and outliers, and provides interpretability in the DR result.

3 ALGORITHM ARCHITECTURE

Fig. 1 shows a general architecture of the back-end of MuTiDR. MuTiDR provides two major functionalities: (a) two-step DR to project a third-order tensor onto a low-dimensional space and (b) generation of essential information for interpreting the two-step DR results.

3.1 Two-Step DR

We describe how MuTiDR achieves the projection of a third-order tensor. To make an explanation concrete and concise, we use a case shown in Fig. 1a. The descriptions below related to T time points, N instances, and D variables are interchangeable between themselves.

The first step of DR is to compress a third-order tensor $\mathbf{X} \in \mathbb{R}^{T \times N \times D}$ into a matrix $\mathbf{Y} \in \mathbb{R}^{N \times T}$, where certain information (e.g., variances) of variables is preserved as much as possible. To achieve this, we first apply *tensor unfolding* [32] along a variable mode (Fig. 1-a①), which reshapes \mathbf{X} to a matrix \mathbf{X} of $(N \times T)$ rows and D columns by arranging all vectors (or often called *fibers*) of D length obtained through the slicing of \mathbf{X} along both time and instance modes. Afterward, we apply a DR method to \mathbf{X} and reduce D dimensions to 1 dimension (Fig. 1-a②). Note that the similar approach is used in Unfold PCA [30, 31] to produce a matrix of $(N \times T)$ rows and D' columns where $D' < D$ and D' is typically two or more as its purpose is obtaining the DR result with one step, unlike our two-step DR. Now, \mathbf{X} is compressed into a vector \mathbf{y} of length $(N \times T)$. Based on \mathbf{y} ’s indexes correspond to the time and instance directions of \mathbf{X} , we can fold \mathbf{y} into a matrix $\mathbf{Y} \in \mathbb{R}^{N \times T}$ (Fig. 1-a③). Because the main purpose of the first DR is preserving the information of variables, a linear DR method that can be used for data compression is suitable. For example, while we can use PCA to preserve the variances of variables, linear discriminant analysis (LDA) is also a potential option if the analyst wants to preserve differences between \mathbf{X} and another third-order tensor. Also, the linearity of DR is important to provide interpretability, as described in Sect. 3.2.

The second step of DR is to visualize \mathbf{Y} in a lower-dimensional space. For this step (Fig. 1-a④), based on the analysis purpose, we can simply select any DR method that can be applied to a matrix, such as PCA and t-SNE [52]. Through this step, $\mathbf{Y} \in \mathbb{R}^{N \times T}$ can be represented as $\mathbf{Z} \in \mathbb{R}^{N \times T'} (T' < T, \text{ typically } T' \in \{1, 2, 3\})$.

Instead of using the two-step DR above, similar to Unfold PCA [30, 31], another potential approach is unfolding \mathbf{X} to a matrix of N rows

and $(D \times T)$ columns and then apply DR in order to reduce dimensions of $(D \times T)$ to a lower number of dimensions. When compared with this approach, the two-step DR has the main advantage in handling different modes (e.g., variables and time points) with clear distinction, and this benefits both identification and interpretation of patterns in \mathbf{X} . For example, when the analyst wants to review the similarities of N instances mainly based on patterns seen along a time mode but not a variable mode, they can use the process shown in Fig. 1a. Also, as described in the next subsection, the interpretation of the DR results becomes more straightforward because, for example, we can understand which time points highly contribute to the characteristics of a cluster seen in the DR result. We provide more detailed comparisons in Sect. 6.

There are six different combinations to generate the two-step DR result \mathbf{Z} based on which modes are selected as the first and second DR targets: (1st DR target mode, 2nd DR target mode) = {(time, instance), (time, variable), (instance, time), (instance, variable), (variable, time), (variable, instance)}. The analyst can choose a preferable combination from these based on their analysis interest. For example, when selecting (variable, time), a two-step DR result shows instance similarities mainly based on temporal behaviors while considering distribution differences in variables. On the other hand, a selection of (variable, instance) generates time points' similarities based on instances' states (i.e., values of the compressed variables each instance has) at each time point.

3.2 Supporting Interpretability

When analyzing the DR result, we often want to identify clusters from the DR result and understand the characteristics of the clusters [11, 21, 42]. Similar to the existing DR methods, identification of clusters can be visually performed on the two-step DR result (i.e., finding a set of points placed closely to each other). However, when compared with the case of applying ordinary DR methods to a matrix, understanding the cluster's characteristics from a two-step DR result is more complicated. Therefore, we provide algorithmic support for this task.

As shown in Fig. 1b, MulTiDR provides two different pieces of information for the interpretability: \mathbf{a} , feature contributions of T time points to a cluster's characteristics, and \mathbf{w} , a parametric mapping used to compress D variables into one dimension.

To obtain feature contributions \mathbf{a} , we follow the contrastive learning (CL) based approach introduced by Fujiwara et al. [21]. As shown in Fig. 1-b①, MulTiDR first takes K instance indices related to a target cluster and then, from \mathbf{Y} , extracts $\mathbf{Y}_K \in \mathbb{R}^{K \times T}$, a submatrix corresponding to these K instances, and $\mathbf{Y}_R \in \mathbb{R}^{(N-K) \times T}$, the rest of \mathbf{Y} (i.e., $\mathbf{Y}_R = \mathbf{Y} \setminus \mathbf{Y}_K$). From inputs \mathbf{Y}_K and \mathbf{Y}_R , CL generates $\mathbf{a} \in \mathbb{R}^T$ (Fig. 1-b②), which shows how strongly each time point contributes to the uniqueness of a target cluster with respect to the others. By referring to \mathbf{a} , the analyst knows which time points in \mathbf{Y} they should review to understand the target cluster's characteristics.

However, each cell of \mathbf{Y} represents the compressed variable from D to 1 dimension. To understand the cluster's characteristics, we also need to know how the compressed variable is derived from the original D variables. To do so, we can refer to a parametric mapping vector $\mathbf{w} \in \mathbb{R}^D$ (Fig. 1-b③), which is usually provided by DR methods for data compression (e.g., PCA). \mathbf{w} consists of a weight for each of D variables, which is used to project D variable values to one compressed value.

3.3 Implementation Example

As described above, the back-end architecture of MulTiDR provides flexibility in the selection of the first DR, second DR, and CL. This flexibility enables MulTiDR to support various analysis needs, as discussed in Sect. 3.1. Here, we describe a representative implementation example, which we use through the rest of the paper. For the first DR, we use PCA because it is most popularly used for data compression when applying machine learning methods, including DR methods. We use UMAP [38] as the second DR because of its effectiveness to find patterns from nonlinear relationships. Also, unlike the other nonlinear DR methods (e.g., t-SNE [52]), UMAP is suitable for capturing both local and global topological structures of the data [38]. Because of this ability, UMAP is effective in finding patterns from both small- and large-scale data while many other nonlinear DR methods are not

suitable for small-scale data (e.g., data with 50 instances). Lastly, for the purpose of understanding the characteristics of clusters, currently, ccPCA [21] is the only available option; thus we use it as a CL method.

4 MULTIDR VISUAL INTERFACE

MulTiDR provides a visual interface to support interactive analysis of the two-step DR results together with the information that helps the interpretation of the results. As shown in Fig. 2, MulTiDR visual interface consists of five coordinated views: (a) a two-step DR (TDR) view, (b) a supplemental information (SI) view, (c) a feature contribution (FC) view, (d) a histogram comparison (HC) view, and (e) a projection mapping (PM) view.

Fig. 3 shows an analysis workflow with MulTiDR visual interface. Here, we extend the workflow for high-dimensional data analysis introduced by Fujiwara et al. [21] for multivariate time-series analysis. After obtaining a two-step DR result \mathbf{Z} , feature contributions \mathbf{a} , and a parametric mapping \mathbf{w} , the two-step DR result is visualized in Fig. 2-a. The analyst can first visually identify clusters from the DR result (Fig. 3-A) and then analyze each cluster. When points in the DR result have the auxiliary information (e.g., the location information of instances), the analyst can (B) relate the identified clusters to such information, as shown in Fig. 2-b. Afterward, they can move forward to steps (C, D, E), where the information of feature contributions and parametric mapping is used to understand the clusters' characteristics. With Fig. 2-c, the analyst can start with (C) finding which features (i.e., columns in \mathbf{Y}) highly contribute to characterizing each cluster. For each of the highly contributed features, by using Fig. 2-d, the analyst can (D) compare the differences of feature value distributions among clusters. Since the features are obtained through the compression with the first DR, the analyst also (E) interprets the meaning of the features by reviewing the parametric mapping information provided in Fig. 2-e. As indicated with the arrows in Fig. 3, the above steps often drive a continuous analysis loop in order to identify other clusters, select other features of interest, or examine findings obtained in the other view.

For the rest of section, we describe each view of MulTiDR with a concrete analysis example using the US weekly air quality data in 2018 [50], which consists of 53 weeks, 55 counties, and 5 different air quality measures (i.e., $T = 53$, $N = 55$, $D = 5$). A demonstration video of the interface is available at our online site [1].

4.1 Visualization of Two-Step DR Results

The TDR view (Fig. 2-a) visualizes the results obtained through the two-step DR as scatterplots. As described in Sect. 3.1, the two-step DR can generate six different results from a multivariate time-series dataset based on target modes of the first and second DR (e.g., the first DR along a variable mode and the second DR along a time mode). From these results, the analyst can select which mode's similarities they want to show from a drop-down menu at Fig. 2-f. For example, in Fig. 2-a, instance similarities are selected. Consequently, as described at the top of each of scatterplots (a1 and a2), the TDR view shows two results that are obtained by applying the first and second DR along (variable, time) and (time, variable) at the left and right, respectively.

From the results, the analyst can visually identify clusters and manually select them by using a lasso selection. Selected points are labeled as one cluster and color-coded with a categorical color. For example, in Fig. 2-a1, the analyst has first selected Cluster 1 (blue) and then Cluster 2 (orange). In addition to the lasso selection, TDR view also supports fundamental interactions, such as zooming and panning. After the selection, all other views update their visualizations. From Fig. 2-a1 and a2, we can see that although the orange points in a1 are also relatively placed closely to each other in a2, the clusters in a1 tend to be more mixed with each other in a2. This indicates that instances (i.e., counties) in these clusters generally have similar temporal patterns in their representative variable values (i.e., representative air quality measure); however, they tend to have different patterns in variable values (e.g., some of the blue points may have high variable values but the others do not). We demonstrate an analysis example utilizing both of the two different DR results in Sect. 5.3.

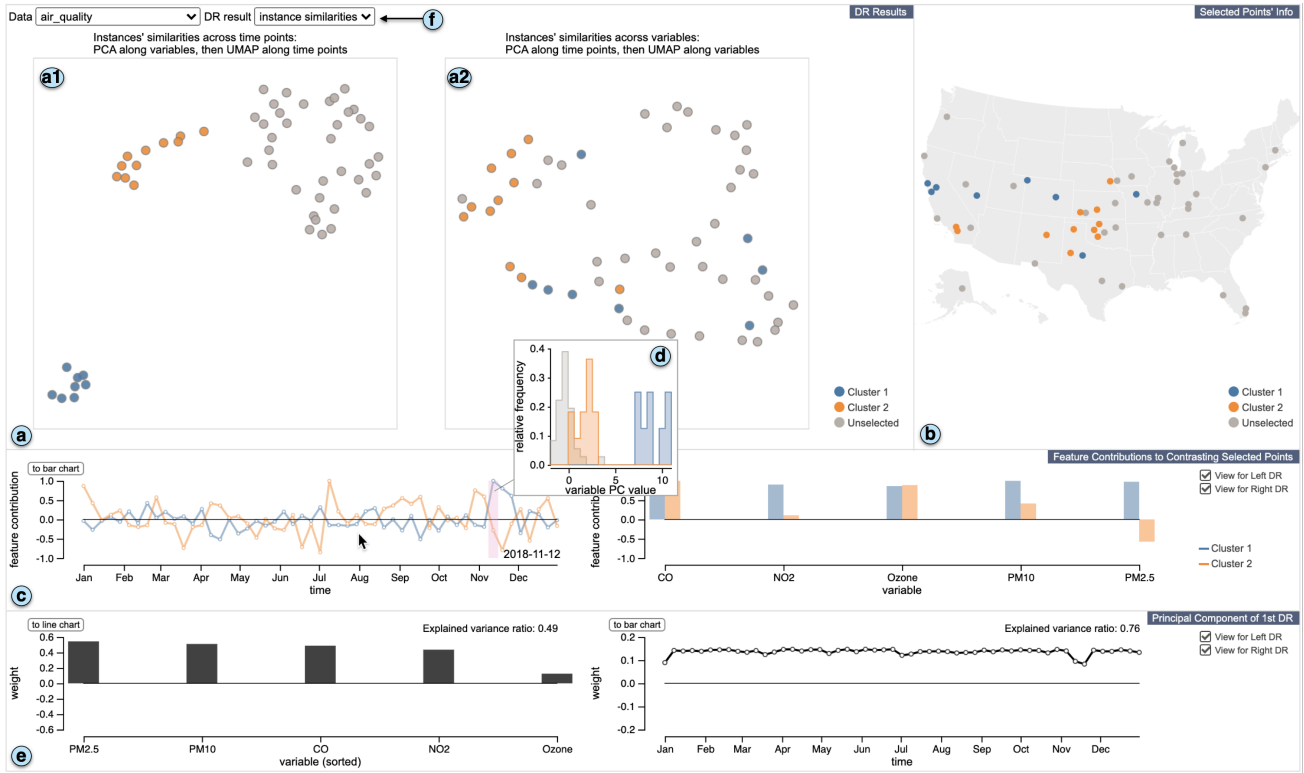


Fig. 2: A screenshot of MultiTiDR visual interface. Here we visualize the AirData [50], air quality data at outdoor monitors across the US, collected in 2018. (a) A two-step DR (TDR) view draws the DR results obtained through the two-step DR. (b) A supplemental information (SI) view supports understanding selected points in the TDR view with the auxiliary information. (c) A feature contribution (FC) view visualizes features (either instances, variable, or time points) and their contributions to characteristics of each of selected clusters. (d) A histogram comparison (HC) view shows the feature values in the first DR result Y of the selected element in (c). (e) A parametric mapping (PM) view depicts parametric mappings generated in the first DR, specifically the mappings to the first principal component in this example. (f) The analyst can select a type of the DR results.

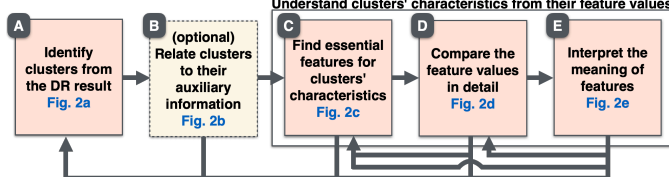


Fig. 3: Multivariate time-series analysis workflow with MultiTiDR visual interface.

4.2 Visualization of Related Contexts

After identifying clusters, we often want to understand what kind of points are included in each cluster and why they are clustered by the two-step DR.

The SI view (Fig. 2-b) is designed for the former task. The SI view visualizes the auxiliary information of the selected points in the TDR view if available. In Fig. 2-b, the location information of the selected counties is visualized, where the blue and orange clusters tend to be seen in more west and center, respectively. MultiTiDR provides a set of predefined visualizations and selects one from them based on which mode and dataset need to be visualized. For example, when showing the information for a time mode of the air quality data, MultiTiDR shows a calendar-based visualization to convey the seasonal patterns. While the SI view shows the location information for an instance mode of a geospatial dataset, when analyzing a network data, the SI view can provide a node-link diagram. We demonstrate examples in Sect. 5.

4.3 Visualization of Feature Contributions and Values

In the next step, the analyst can analyze the clusters' characteristics with the FC view (Fig. 2-c) and HC view (Fig. 2-d).

The FC view shows feature contributions a for each of DR results in the TDR view (the left and right plots in Fig. 2-c correspond to Fig. 2-a1 and a2, respectively). In default, line charts are employed for feature contributions of time points, while bar charts are used for

those of instances or variables. However, the analyst can switch line and bar charts by clicking the button placed at the top of each of y-axes (e.g., “to bar chart” at the left side of the Fig. 2-c). Also, with the check boxes placed at the far right in Fig. 2-c, the analyst can select showing only one of the plots to use more screen space. Since we obtain feature contributions for each cluster, we visualize them with the corresponding cluster color. MultiTiDR scales feature contributions between $[-1, 1]$ by dividing each set of feature contributions by their maximum absolute value. Closer to either 1 or -1 indicates higher contributions to the characterization of a cluster. The meaning of the sign is discussed in Sect. 4.3.1. For features that have high contributions, each cluster likely has different distributions from the other points.

To compare value distributions of the selected feature, as shown in Fig. 2-d, the HC view shows relative frequency histograms of selected clusters (e.g., blue and orange) and unselected points (gray) with the corresponding colors. The x-axis of the histograms represents feature values (i.e., cell values in Y). The y-axis shows relative frequency—ratio of the number of items in each bin to the total number of items across all bins—within each group and its maximum limit is set to the maximum relative frequency among the histograms. From the result in Fig. 2-d, at the selected week highlighted with pink (i.e., a week of November-12th, 2018), the blue cluster tends to have much higher feature values than the others.

4.3.1 Sign Adjustment of Feature Contributions

ccPCA [21], which is used as a default CL method in MultiTiDR, produces signed feature contributions (FCs). Signed FCs have a strength of differentiating features of having lower and having higher values within a selected cluster. For example, when looking at Cluster 2 (orange) in Fig. 4-a, where the absolute FCs are shown, both time points ③ and ④ have the relatively high FCs; however, as shown in Fig. 4-d, while Cluster 2 tends to have high values at ③, it has low values at ④. On the other hand, the signed FCs shown in Fig. 4-b indicates the difference of time points ③ and ④ (③: negative sign, ④: positive sign).

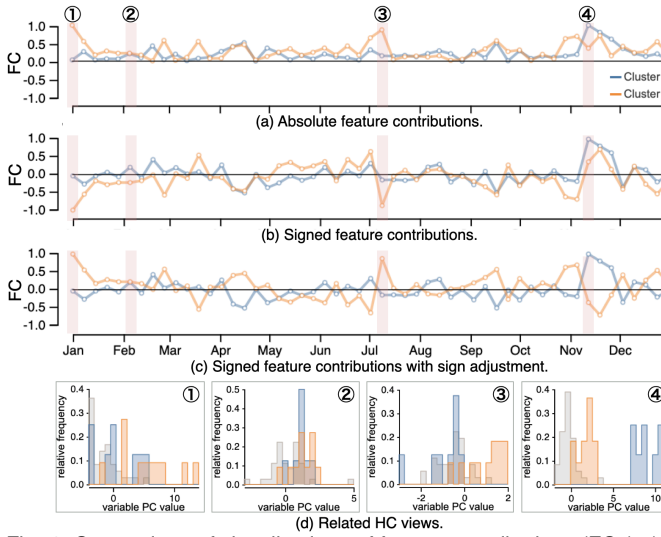


Fig. 4: Comparison of visualizations of feature contributions (FCs): (a) absolute FCs, (b) signed FCs, and (c) signed FCs with sign adjustment. (d) shows the HC views corresponding to the four selected time points ①–④ in (a), (b), and (c).

Despite the usefulness of signed FCs, similar to ordinary PCA, the *sign ambiguity* problem [20,21,49] in ccPCA limits their interpretability. That is, the signs are arbitrarily selected and thus they do not reflect whether features contribute to having higher or lower values than others. For example, in Fig. 4-b, although both Clusters 1 and 2 have similar line shapes and strong positive FCs at ④, as shown in Fig. 4-d, at this time point, Cluster 1 (blue) tends to have high values while Cluster 2 (orange) tends to have low values. Therefore, using the signed FCs directly produced by ccPCA might mislead the analyst (e.g., they consider Clusters 1 and 2 are similar from Fig. 4-b).

To solve the above problem, we introduce a sign adjustment algorithm that optimally matches the directions of sign and value distributions (i.e., when a sign is positive, a cluster tends to have higher feature values than others, and vice versa). First, for each feature, we compute Pearson's correlation coefficient r ($-1 \leq r \leq 1$) between all points' cluster memberships (i.e., 0: points are non-members, 1: points are members of the selected cluster) and their feature values. When r is closer to 1, members of the cluster more likely have a higher feature value than non-members. On the other hand, closer to -1 , higher possibility to have a lower feature value. We denote a set of r for all features as a vector \mathbf{r} . Next, we compute a score of agreement s between correlation coefficients \mathbf{r} and signed FCs \mathbf{a} by taking their dot product (i.e., $s = \mathbf{r} \cdot \mathbf{a}$). s increases when an element of \mathbf{r} and the corresponding element of \mathbf{a} have the same signs, while s decreases when they have the opposite signs. Also, the magnitudes of elements of \mathbf{r} and \mathbf{a} can be considered as weights to decide how much s should increase or decrease. As a result, s becomes a higher positive value when each pair of elements of \mathbf{r} and \mathbf{a} has higher magnitudes of r and FC with the same signs. When $s < 0$, \mathbf{r} and \mathbf{a} disagree with each other; thus, we flip signs of all elements in \mathbf{a} .

The result after applying the sign adjustment is shown in Fig. 4-c. Now, we can see that Clusters 1 and 2 have clearly different patterns in FCs. For example, while Cluster 1 has a strong positive FC at ④, Cluster 2 has strong positive FCs at ① and ③ and a strong negative FC at ④. Also, by referring to the HC views in Fig. 4-d, these differences well represent differences in the distributions of feature values. For instance, at ①, Cluster 2 tends to have high feature values but low feature values at ④, while Cluster 1 has high feature values at ④. With the sign-adjusted FCs, to understand the differences between clusters, the analyst can mainly focus on reviewing features that have much different contributions between clusters.

Note that the work that introduced ccPCA [21] also presented a sign adjustment algorithm to deal with the inconsistency of signs of FCs across clusters. However, our algorithm focuses on matching the directions of sign and value distributions for each cluster to ensure that

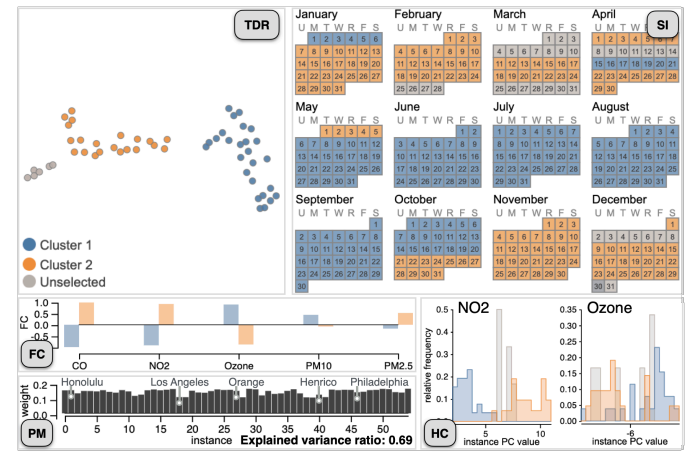


Fig. 5: Case study 1. (TDR) shows similarity of each week's air quality measures. (SI, FC, PM) are the SI, FC, PM views after selecting Clusters 1 and 2 in the TDR view, respectively. (HC) shows the HC views when selecting "NO2" and "Ozone" form (FC).

a cluster has high feature values when its feature has a strong positive FC.

From the result shown in Fig. 2-c(left), now we know Cluster 1 tends to have high feature values around the middle of November but low feature values around the middle of April. Also, we can see that Cluster 2 tends to have the opposite patterns from Cluster 1.

4.4 Visualization of Parametric Mappings

The last analysis step is to understand the meaning of features obtained after the first DR of the two-step DR (i.e., columns in \mathbf{Y}). To support this task, the PM view (Fig. 2-e) visualizes a vector of parametric mapping \mathbf{w} for each of the DR results as either line or bar chart, as similar to the FC view. Note that \mathbf{w} is common across all points, and thus all lines or bars are colored in black. Also, using texts, at the top-right corner of each plot in the PM view, we inform the quality of the first DR (e.g., *explained variance ratio* provided by many linear DR methods such as PCA and LDA). From Fig. 2-e(left), we can see that the feature values are generated with similar weights for all measures except for "Ozone". Therefore, we can interpret the feature values in Fig. 2-d are close to the mean of "PM2.5", "PM10", "CO", and "NO2".

4.5 Implementation

We have developed MultiDR as a web application. For the back-end of MultiDR¹, including the algorithms described in Sect. 3, the sign adjustment algorithm in Sect. 4.3.1, and the generation of histogram information for the HC view, we use Python to integrate all the existing implementations, such as UMAP [38] and ccPCA [21]. The front-end visual interface is implemented with a combination of HTML5, JavaScript, D3 [10], and WebGL. We use WebSocket to communicate between the front-end and back-end.

5 CASE STUDIES

We have shown the effectiveness of MultiDR through the analysis of the air quality data in US [50]. Here we further analyze the same data from different aspects. Additionally, we demonstrate three additional case studies, including analyses of a body sensing dataset, a dynamic social network, and supercomputer's hardware logs. For each study, we have preprocessed each dataset to deal with its missing values or extract useful information for the analysis. All the processed datasets except for the supercomputer's hardware logs (due to its confidentiality) and parameters used for each DR result are available in our online site [1].

5.1 Study 1: Analysis of US Air Quality Data

Analysis of Weekly Patterns of Air Quality Measures. In Sect. 4, we have analyzed the clusters of instances (i.e., US counties) selected in Fig. 2-a1; here, we analyze the similarities of time points (weeks in

¹The source code is partially available from our online site [1]

2018) based on their values of air quality measures. For this task, we apply the two-step DR using PCA along an instance mode (i.e., counties) and then UMAP along a variable mode (i.e., air quality measures). The generated results are shown in Fig. 5.

From the TDR view shown in Fig. 5-TDR, we select several clearly separated points (i.e., weeks) as clusters. For this data, the SI view provides a calendar-based visualization and indicates the corresponding weeks for each cluster (Fig. 5-SI). We notice that while the blue cluster generally relates to the weeks from May to the middle of October, the orange cluster consists of the weeks from the late fall to the early spring. To understand differences of each cluster, we refer to the FC view in Fig. 5-FC. The two clusters have quite different FCs, and thus seem to have different feature values as well. For example, in the histograms of “NO₂”, as shown in Fig. 5-HC, Clusters 1 (blue) and 2 (orange) tends to have low and high feature values when compared with others, respectively. On the other hand, in the histograms of “Ozone”, we can see the opposite distributions. From the PM view (Fig. 5-PM), we can see that several counties (e.g., Honolulu) have slightly higher weights than others when generating the feature values.

In general, we can conclude that the air quality data has seasonal changes, such as “Ozone” has higher values around the summer (blue weeks) when compared with around the winter (orange weeks).

5.2 Study 2: Analysis of MHEALTH (Mobile Health) Dataset

In this case study, we analyze the MHEALTH (Mobile HEALTH) [8, 9] dataset. This dataset consists of physical recordings of motion and vital signs for ten volunteers while performing twelve physical activities. Sensors are placed on the subjects’ chest, wrist, and ankle. The measurements taken from sensors include movement experienced by different body parts, such as acceleration with the magnitude for each of X-, Y- and Z-directions. The sensor modalities are recorded at a sampling rate of 50 Hz. The dataset contains points that represent bursts of highly active minutes.

Study 2-1: Categorization of Physical Activity Measurements. As shown in Fig. 6, from the TDR view (Fig. 6-TDR), where variables’ (i.e., measurements’) similarities are shown by applying PCA and UMAP along instance and time modes, respectively, we select Cluster 1–2 (blue and orange). The SI view in Fig. 6-SI lists all measurements related to each cluster as texts.

Afterward, we review the related information with the FC, PM and, HC views (Fig. 6-FC, PM, HC). From Fig. 6-FC, we can see that, across time, blue and orange clusters have strong positive and negative FCs, respectively. To further investigate, we select several timestamps and review the corresponding histograms. Fig. 6-HC shows the histograms at two examples of the selected timestamps (① and ②). From the results shown in Fig. 6-HC, all the measures within each cluster tend to have close feature values (e.g., in ①, all orange points have the low feature values). By looking at Fig. 6-PM, PCA seems to generate the feature values with higher weights for Subjects 5–9 when compared to Subjects 0–4 with an explained variance of 0.45.

From the observations above, we can say that all the measures in Cluster 2, which includes the accelerations of the chest (X-direction), the left-ankle (Y-direction), and the right-arm (X- and Y-directions) have similar value distributions for each timestamp. The same applies to the measures in Cluster 1.

Study 2-2: Classification of Temporal Patterns among Subjects. Next, we analyze the similarities of time points in the duration of activity measurement (10 minutes). During the measurement, the subjects performed an activity set, including standing still, walking, running, etc. We apply the two-step DR using PCA along a variable mode and then UMAP along an instance mode. The generated results are shown in Fig. 7. From the TDR view shown in Fig. 7-TDR, we select multiple clearly separated clusters. In the SI view (Fig. 7-SI), we see that each cluster is gathered together with a range of about 1 minute. Since the subjects were asked to perform each activity with a duration of approximately 1 minute for collecting data, we can expect that each cluster well represents each of the activities.

To understand the differences of each cluster, we refer to the other views (Fig. 7-FC, HC, and PM). All clusters have quite different FCs in

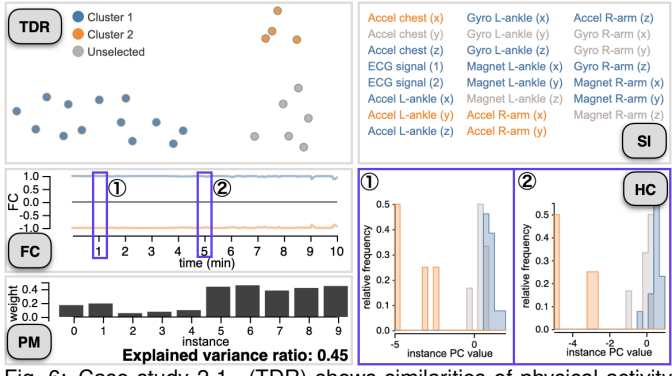


Fig. 6: Case study 2-1. (TDR) shows similarities of physical activity measurements based on their temporal behaviors. (FC, PM) are the FC and PM views after selecting two clusters from (TDR). (HC) shows the HC views after selecting two different timestamps from (FC).

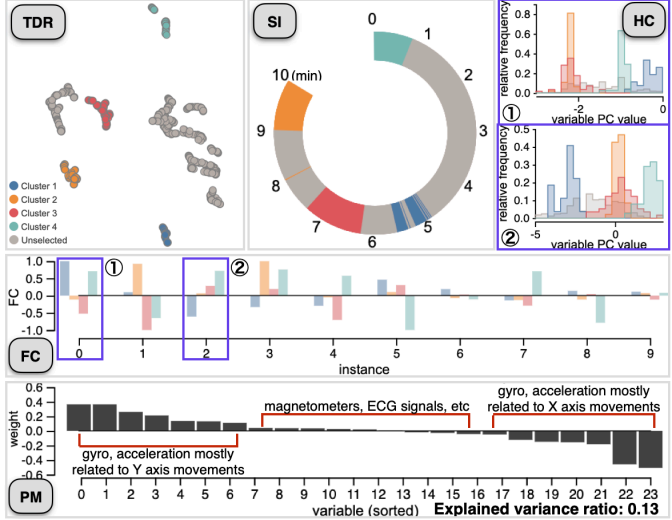


Fig. 7: Case study 2-2. (TDR) shows similarities of timestamps based on subjects’ activities. (SI) visualizes the corresponding time information with a circular layout. (FC, PM) are the FC and PM views after selecting four clusters from (TDR). (HC) shows the HC views after selecting two different instances from (FC).

Fig. 7-FC. Also, by referring to the HC views, as the examples in Fig. 7-HC show, each subject tends to have quite different feature values. For example, while Subject 0 (annotated with ①) tends to have high feature values during the activity corresponding to Cluster 1 (blue), Subject 2 (annotated with ②) tends to have low feature values for Cluster 1. From the PM view, we understand that the feature values mainly relate to the measures of gyroscopes and accelerations but not magnetometers or ECG signals. More specifically, the measures related to Y-directions (e.g., “gyro R-forearm (y)”, “gyro L-ankle (y)”, “acceleration chest (y)”) tend to have positive weights, while the measures of X-direction have negative weights.

Therefore, we can conclude that, in general, the two-step DR successfully separates time points related to a specific activity based on the differences of each activity in the measures of X- and Y-directions.

5.3 Study 3: Analysis of Dynamic Contact Networks

Here, we provide an analysis example of dynamic networks, using a dataset of contacts between high school students in Marseilles, France [18]. This dataset contains network links, which represent the students’ face-to-face contacts collected with 20-second intervals for several days. We constructed temporal snapshots from this dynamic network by aggregating contacts within a time window of 5–9 AM, 10 AM–12 PM, 1–3 PM, 4–6 PM, or after 6 PM for each day. This procedure generated 30 snapshots (i.e., networks) of 180 students (i.e., nodes) with the mean of 193 contacts (i.e., links). To extract features of network nodes, we applied DeepGL [44], a network representation

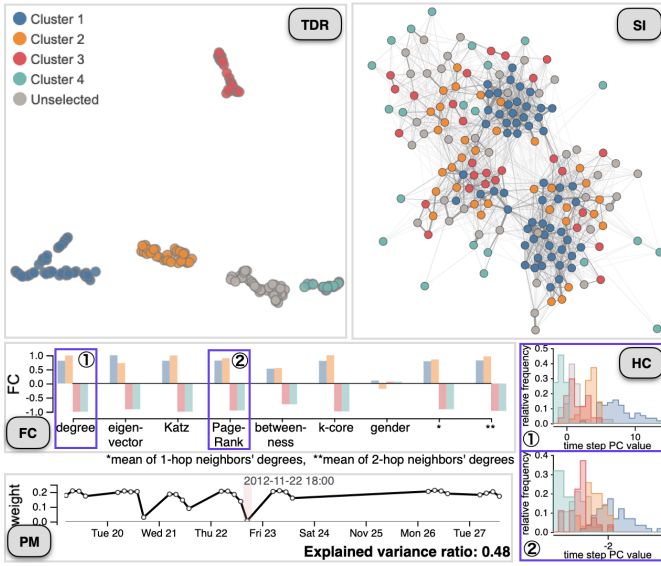


Fig. 8: Case study 3-1. (TDR) shows similarities of the students based on their node features obtained with DeepGL [44]. (SI) draws a node-link diagram of the entire contact network. (FC, PM) are the FC and PM views after selecting four clusters from (TDR). (HC) shows the HC views after selecting two different node features from (FC).

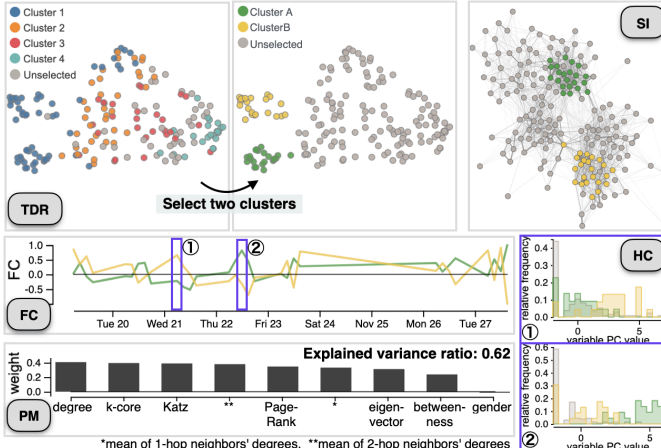


Fig. 9: Case study 3-2. (TDR) shows similarities of the students based on their temporal behaviors. From the result at the left, where the colors correspond to the selection in Fig. 8-TDR, we select Clusters A and B at the right. (SI, FC, PM) are the SI, FC, and PM views after selecting the two clusters. (HC) shows the HC views after selecting two different timestamps from (FC).

learning method that produces features consisting of node attributes (e.g., gender), network centralities (e.g., degree centrality [41]), network measures (e.g., k -core number [41]), and those of statistical values of neighbors (e.g., the mean degree centrality of 1-hop neighbors). As a result, we obtained a tensor of $T = 30$, $N = 180$, and $D = 10$.

Study 3-1: Categorization of Students Based on Node Features. Fig. 8-TDR shows a result generated by the two-step DR using PCA along a time mode and UMAP along a variable mode (i.e., the dots in the TDR view represent instances). The result contains five distinct clusters and we select four of them. The resultant visualizations are shown in Fig. 8-SI, HC, FC, and PM. Here, the SI view draws an overall network constructed using a time window of the entire measurement period. From Fig. 8-SI, we notice that the blue nodes (i.e., students) in Cluster 1 can be seen in the strongly connected regions. In contrast, the teal nodes in Cluster 4 have only a small number of links to the others.

To further understand each cluster's characteristics, we review the FC view (Fig. 8-FC). We can see that, except for "gender", generally Clusters 1 and 2 have strong positive FCs, while Clusters 3 and 4 have strong negative FCs. In the HC views (Fig. 8-HC), which show the

histograms of ① degree and ② PageRank, Clusters 1 and 2 tend to have higher values than Clusters 3 and 4. Especially, Cluster 1 has much higher values than the others. From the PM view (Fig. 8-PM), we can see that the features in the FC view are generated by using large weights around mornings whereas evenings have close to zero weights (e.g., 6 PM on November 22nd, as highlighted). This indicates that the first DR (i.e., PCA) has effectively selected time points where the students more actively contacted each other.

With the above analysis, we can conclude that during school hours, the students in Cluster 1 played a central role in communications among students as they have high values for various network centralities.

Study 3-2: Categorization of Students Based on Temporal Communication Patterns. Together with the results in Study 3-1, we further review the instance similarities obtained by applying PCA along a variable mode and UMAP along a time mode. Fig. 9-TDR(left) shows the two-step DR result colored based on the selection in Fig. 8-TDR. We can see that each of the currently selected clusters is generally arranged from left to the right. However, most students in Cluster 1 are separated into two distinct clusters in the far left. We select the two clusters as Clusters A (green) and B (yellow), as presented in Fig. 9-TDR(right). In the SI view (Fig. 9-SI), these two clusters are clearly separated into the two strongly connected regions at the top and bottom. The FC view (Fig. 9-SI) shows that the two clusters have different patterns in FCs across time. We select two clear peaks, ① (Wednesday morning) and ② (Thursday noon), to see their value distribution differences with the HC view (Fig. 9-HC). We can see that Clusters A and B tend to have high feature values at ② and ①, respectively. By looking at the PM view (Fig. 9-PM), the feature values represent the network centralities and measures but not the gender.

From the above observations, we can say that the students in Cluster 1 (the central role of the communications) can be further categorized into two different groups, Clusters A and B, which had active communications at the different time periods.

5.4 Study 4: Analysis of Supercomputer Hardware Logs

In this study, we analyze hardware logs obtained from a supercomputer. Supercomputers are required to have high robustness and reliability to continuously run large-scale computations. Analyzing their hardware logs is fundamental to revealing and understanding abnormal hardware behaviors (e.g., extreme increases of CPU temperatures), which can lead to hardware failures or errors [23, 46].

Here, we specifically review the K computer's [39] hardware logs on January-12th, 2017. The logs were obtained from 864 compute racks, where 1,163 different measures (e.g., CPU temperatures, circuit voltages, and cooling fan spin speeds) are collected every 5 minutes (i.e., 1,440 timestamps in a day). Therefore, the logs can be represented as a $T \times N \times D$ tensor where $T = 1,440$, $N = 864$, and $D = 1,163$ (in total, more than 1.4 billion elements). Through this case study, we demonstrate how MulTiDR helps the analyst identify and characterize outliers from an extremely large-scale dataset.

Study 4-1: Identification and Characterization of Outlier Racks. As a first analysis, we identify racks that have unusual temporal behaviors. To achieve this, we apply the two-step DR with PCA along a variable mode and then UMAP along a time mode (i.e., the dots in the TDR view represent instances). The visualized DR result is shown in Fig. 10-TDR. We can see that while there is a large cluster that contains many racks (the gray points placed at the right side), some racks form small distinct clusters from the main cluster. We select three of these small clusters (Clusters 1–3) in Fig. 10-TDR. Because these outlier clusters could relate to a specific physical location (e.g., a parallel application is often allocated to run in a specified location), we refer to the SI view (Fig. 10-SI), where the physical coordinates of racks are visualized; however, these clusters seem not to fit such a case.

To understand the clusters' characteristics, we analyze the results with the FC, HC, and PM views (Fig. 10-FC, HC, PM). In Fig. 10-FC, we first see that, across time, Clusters 1, 2, and 3 generally have moderate, strong negative, and strong positive FCs, respectively. From Fig. 10-FC, we select Timestamp ① as a sample timestamp following this general pattern and two timestamps (② and ③) that have a unique

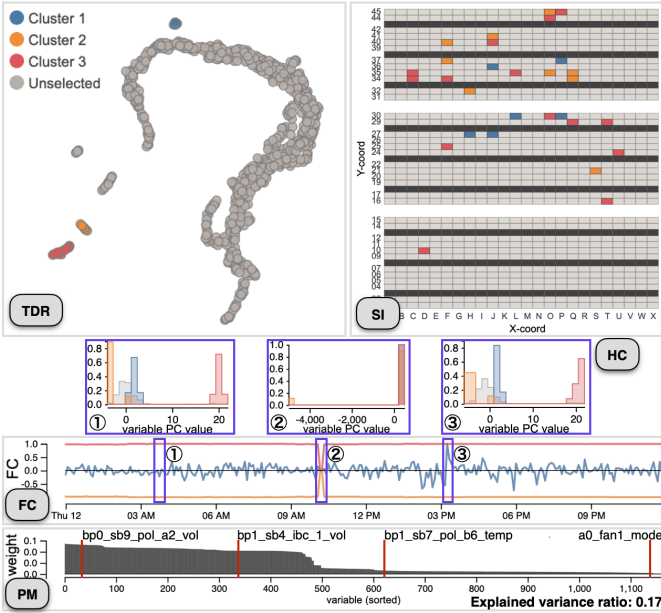


Fig. 10: Case study 4-1. (TDR) shows similarities of racks based on their temporal behaviors. (SI) visualizes the racks' physical coordinates in the K computer. (FC, PM) are the FC and PM views after selecting three outliers from (TDR). (HC) shows the HC views after selecting three different timestamps from (FC).

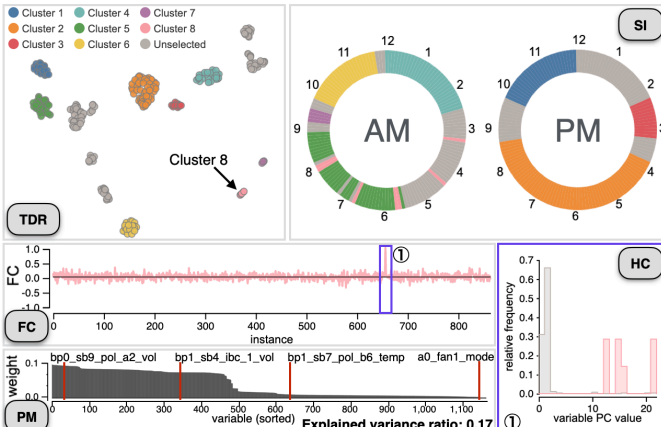


Fig. 11: Case study 4-2. (TDR) shows similarities of timestamps based on behaviors of racks at the corresponding time. (SI) informs the selected timestamps with a clock-based visualization. We show the more information of Cluster 8 in the FC, PM, and HC views (FC, PM, HC).

shift of the FCs. By looking at the HC view of Timestamp ①, we observe that Cluster 3 (red) has much higher feature values than the others, while Clusters 1 (blue) and 2 (orange) have slightly higher and lower feature values than the main cluster (gray), respectively. However, at Timestamp ②, all the racks have similar feature values. At Timestamp ③, when compared with Timestamp ①, Cluster 1 has slightly less overlaps with the gray bins. Next, we review the PM view (Fig. 10-PM), where 1,163 measures' weights are shown, and notice that only the first 500 measures have weights not close to zero. By showing these measures' names by hovering a mouse, we know that the first 500 measures are related to the voltages ("vol") but not the others, including the temperatures ("temp") and fan information ("fan_mode").

Therefore, we can conclude that, across time except for around 10 AM, the racks in Cluster 3 had extremely high voltages while Cluster 1 and 2 had slightly higher and lower voltages than most of the racks.

Study 4-2: Identification and Characterization of Outlier Timestamps. Next, we identify timestamps, at which racks had different behaviors from a usual state, by reviewing the two-step DR result generated by applying PCA along a variable mode and then UMAP along an instance mode (i.e., the dots in the TDR view represent timestamps).

The visualized results are shown in Fig. 11.

From Fig. 11-TDR, we select several distinct timestamp clusters (Clusters 1–8). In the SI view (Fig. 11-SI), where the corresponding timestamps are shown with a clock-based visualization, we can see most clusters relate to the specific time range (e.g., timestamps in Cluster 3 are seen from about 2 to 3 PM). We can consider that each of these clusters corresponds to the duration when performing an allocated job. However, we can see that Cluster 8 is separated in several short time ranges in AM. Since this pattern might relate to the abnormal behavior, we further review Cluster 8 by using the FC, PM, and HC views. From Fig. 11-FC, we can see that Cluster 8 has a strong positive FC for one instance (i.e., rack), as annotated with ①. By looking at the HC view, we can see that, for this instance, the timestamps belonging to Cluster 8 have a much higher feature value than the other timestamps (note: here the gray bins include all the timestamps except for those in Cluster 8). Since the parametric mapping is the same as Study 4-1, we can say that these feature values mainly represent multiple voltage measures. Therefore, Cluster 8 is considered as outlier timestamps by the two-step DR because one specific rack had extremely high voltages at the corresponding timestamps.

6 QUALITATIVE COMPARISON

The two-step DR in MultiDR employs data compression with DR to produce a matrix from a third-order tensor. Instead, as discussed in Sect. 3.1, we can simply apply tensor unfolding along one mode to generate a matrix and then perform DR on such a matrix (e.g., applying DR on a matrix of N rows and $(D \times T)$ columns to visualize instance similarities). Another option is computing statistical measures, such as mean values, when generating a matrix from a third-order tensor. MultiDR contains this approach if we consider the computation of statistical measures as one of DR methods that generates a representative value. Here, we compare three different methods above and discuss the advantages of the two-step DR.

More specifically, we compare two different implementations of the two-step DR, (1) using PCA for the first DR and UMAP for the second DR (we call this method *PCA & UMAP*) and (2) using the mean computation for the first DR and UMAP for the second DR (*Mean & UMAP*), and (3) the unfolding approach (i.e., without the first DR step) using UMAP as a DR method (*Unfolding & UMAP*). We apply these methods to the datasets we analyze in Sect. 4 and 5.

Fig. 12 shows the DR results. Here, we manually select several distinct clusters from the results of PCA & UMAP and then color-code the corresponding points in the other views based on the cluster information. In general, some of the findings described in Sect. 5 from the results of PCA & UMAP cannot be uncovered with either using Mean & UMAP or Unfolding & UMAP.

PCA & UMAP vs Mean & UMAP. Mean & UMAP generates similar results with PCA & UMAP when PCA & UMAP generates a projection mapping consisting of almost uniform weights (e.g., the results for the US air quality dataset); however, for the other cases, Mean & UMAP does not show several meaningful clusters and outliers or does not clearly discern them from the other points. A concrete example can be seen in the instances' similarities of the supercomputer hardware log in Fig. 12-a, where the result of Mean & UMAP mainly shows a single cluster and does not reveal the outlier clusters found with PCA & UMAP. Also, unlike PCA & UMAP, the result in Fig. 12-b does not provide a clear separation of time points that are related to different physical activities. When a target mode of the first DR has significant differences in variances for each index (i.e., a variable, an instance, or a time point), PCA & UMAP can preserve more variety along the mode, and thus PCA & UMAP would produce more useful results. However, again, the two-step DR does not restrict a DR method used for the first DR and allows the analyst to select a preferable compression/feature selection method, including the mean computation, PCA, LDA, etc.

PCA & UMAP vs Unfolding & UMAP. Unfolding & UMAP has quite different results from the ones with PCA & UMAP and seems to fail to find several clusters and outliers. For example, in the time points' similarities of the US air quality dataset (Fig. 12-c), while PCA & UMAP shows the clusters that represent the seasonal air quality

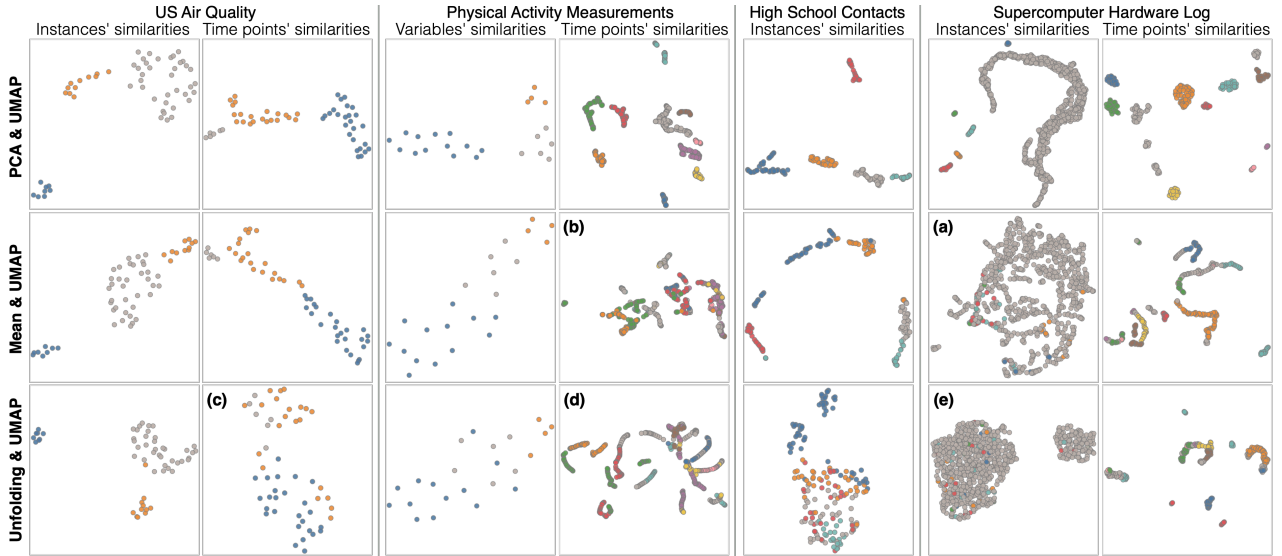


Fig. 12: Visual comparison of the DR results. Colors represent clusters selected in the result of PCA & UMAP.

change (as described in Sect. 5.1), Unfolding & UMAP does not clearly display such clusters. Moreover, similar to Mean & UMAP, the result in Fig. 12-d does not clearly discern different physical activities. Also, Fig. 12-e does not uncover the outlier clusters seen in the result with PCA & UMAP. This limitation of Unfolding & UMAP relates to the fact that Unfolding & UMAP mixes two different modes together and, as a result, it cannot discover the patterns highly related to a specific mode. Another major drawback of Unfolding & UMAP is that it makes the characterization of clusters more difficult because of the complexity of features in the FC view, where each feature represents a mix of two modes (e.g., variables \times instances), and the massiveness of the number of features (e.g., the supercomputer log dataset of $D = 1,163$ and $N = 864$ generates $D \times N = 1,004,832$ features).

7 DISCUSSION

We have evaluated MuTiDR with the case studies and qualitative comparison. Through the qualitative comparison, we have discussed the strength of the two-step DR when compared with the other approaches. Here, we provide an additional discussion from different aspects.

Limitations of Visual Scalability. In MuTiDR’s visual interface, we overlay multiple charts in the FC view and the HC view to make comparison of different clusters’ FCs and feature value distributions easier. However, when many clusters are selected (e.g., ten clusters), these visualizations could cause too many overlaps and clutters. To deal with such a situation, we can provide a visual comparison using small multiples and allow the analyst to select either overlays or small multiples based on their preference.

Also, when each mode has many dimensions, it becomes difficult to grasp what kind of dimensions has high FCs and weights from the FC and PM views, respectively. This is especially problematic when x -axis of the FC or PM view represents a variable mode because it often consists of variables that have different types of measures (e.g., network routers’ temperatures, voltages, sent, and received packets). For this issue, before visualizing the information of a variable mode, we can consider applying aggregation based on their similarities or available external information (e.g., a class of measures, such as physical loads, including temperatures and voltages, and network loads on routers, including sent and receive packets).

Limitations of the Two-Step DR. The two-step DR is mainly limited by the first DR step. Because this step compresses a target mode into 1D, when the mode has many dimensions (e.g., 1,000 variables in a variable mode), a large amount of information could be lost. However, at the same time, the analyst can check how much of the information is preserved by referring to a quality measure provided by each DR method, such as explained variance ratio in PCA and LDA. When the quality is extremely low (e.g., explained variance ratio is smaller than 0.01), the analyst can consider selecting a subset of dimensions for

their analysis. In addition, to inform the second DR’s quality, we plan to incorporate several model-agnostic quality measures [34, 53] and visualizations [19, 56] in the future.

Generality of the Two-Step DR. The back-end algorithms described in Sect. 3 are used to obtain and understand a low-dimensional representation of multivariate time-series data. However, these algorithms can be applied to other types of data that can be formed into a third-order tensor. For example, even when analyzing single-time-point multivariate data, the analyst may want to separate variables into two different modes, such as patients’ demographics (e.g., ages) and their medical tests (e.g., blood pressures) for an analysis of medical datasets. In such a usage, MuTiDR’s algorithms can help the analyst avoid mixing the influences from two different types of variables on the DR result.

Additional Enhancement for Time-Series Analysis. Through this paper, we have demonstrated the effectiveness of MuTiDR using PCA, UMAP, and ccPCA as the first DR, second DR, and CL methods, respectively. We also can use representation learning methods that focus on time-series analysis. For example, instead of PCA, when applying the first DR along a time mode, we are able to use functional PCA [55], which aims to extract representative temporal patterns, or use multivariate singular spectrum analysis (MSSA) [26], which is suitable to find outlier time points. Also, we can design a CL method that is similar to ccPCA by extending a contrastive version of MSSA [17]. Once it becomes available, we can replace ccPCA with such a method.

Visualizations also can be enhanced for time-series analysis. For example, to convey the temporal order of time points in the TDR view’s scatterplots, we can couple the TDR view with the existing visualization methods described in Sect. 2.2, such as methods developed by Bach et al. [6] and van den Elzen et al. [51].

8 CONCLUSION

We have introduced a visual analytics framework, MuTiDR, which enables us to derive and interpret low-dimensional representations of multivariate time-series data by employing a two-step DR and contrastive learning together with interactive visualization. As demonstrated with our case studies, MuTiDR has abilities of identifying and characterizing clusters and outliers from complex datasets. Therefore, MuTiDR provides a new effective approach to demanding tasks of analyzing multivariate time-series data.

ACKNOWLEDGMENTS

This research is sponsored in part by the U.S. National Science Foundation through grant IIS-1741536 and U.S. Department of Energy through grant DE-SC0014917.

REFERENCES

[1] The supplementary materials: Videos, source code, datasets. <https://takanori-fujiwara.github.io/s/multidr/>.

[2] E. Ahmed, I. Yaqoob, I. A. T. Hashem, I. Khan, A. I. A. Ahmed, M. Imran, and A. V. Vasilakos. The role of big data analytics in internet of things. *Computer Networks*, 129:459–471, 2017.

[3] A. B. Alencar, K. Börner, F. V. Paulovich, and M. C. F. de Oliveira. Time-aware visualization of document collections. In *Proc. SAC*, pp. 997–1004, 2012.

[4] B. Bach, P. Dragicevic, D. Archambault, C. Hurter, and S. Carpendale. A review of temporal data visualizations based on space-time cube operations. In *Proc. EuroVis*. Eurographics/IEEE, 2014.

[5] B. Bach, P. Dragicevic, D. Archambault, C. Hurter, and S. Carpendale. A descriptive framework for temporal data visualizations based on generalized space-time cubes. *Computer Graphics Forum*, 36(6):36–61, 2017.

[6] B. Bach, C. Shi, N. Heulot, T. Madhyastha, T. Grabowski, and P. Dragicevic. Time Curves: Folding time to visualize patterns of temporal evolution in data. *IEEE Transactions on Visualization and Computer Graphics*, 22(1):559–568, 2016.

[7] R. Ballester-Ripoll, P. Lindstrom, and R. Pajarola. TTHRESH: Tensor compression for multidimensional visual data. *IEEE Transactions on Visualization and Computer Graphics*, 2019 (Early Access).

[8] O. Banos, R. Garca, J. Holgado-Terriza, M. Damas, H. Pomares, I. Rojas, A. Saez, and C. Villalonga. mHealthDroid: A novel framework for agile development of mobile health applications. In *Proc. IWAAL*, vol. 8868, pp. 91–98. Springer, 2014.

[9] O. Banos, C. Villalonga, R. Garca, A. Saez, M. Damas, J. Holgado-Terriza, S. Lee, H. Pomares, and I. Rojas. Design, implementation and validation of a novel open framework for agile development of mobile health applications. *BioMedical Engineering OnLine*, 14:S6, 08 2015.

[10] M. Bostock, V. Ogievetsky, and J. Heer. D³ data-driven documents. *IEEE Transactions on Visualization and Computer Graphics*, 17(12):2301–2309, 2011.

[11] M. Brehmer, M. Sedlmair, S. Ingram, and T. Munzner. Visualizing dimensionally-reduced data: Interviews with analysts and a characterization of task sequences. In *Proc. BELIV*, pp. 1–8, 2014.

[12] N. Cao, C. Lin, Q. Zhu, Y.-R. Lin, X. Teng, and X. Wen. Voila: Visual anomaly detection and monitoring with streaming spatiotemporal data. *IEEE Transactions on Visualization and Computer Graphics*, 24(1):23–33, 2018.

[13] J. D. Carroll and J.-J. Chang. Analysis of individual differences in multidimensional scaling via an N-way generalization of “Eckart-Young” decomposition. *Psychometrika*, 35(3):283–319, 1970.

[14] J. P. Cunningham and Z. Ghahramani. Linear dimensionality reduction: Survey, insights, and generalizations. *Journal of Machine Learning Research*, 16(1):2859–2900, 2015.

[15] H. Dai, Y. Tao, and H. Lin. Visual analytics of urban transportation from a bike-sharing and taxi perspective. In *Proc. VINCI*, pp. 1–8, 2019.

[16] D. V. Dimitrov. Medical internet of things and big data in healthcare. *Healthcare Informatics Research*, 22(3):156–163, 2016.

[17] A.-H. Dirie, A. Abid, and J. Zou. Contrastive multivariate singular spectrum analysis. In *Proc. Allerton Conference*, pp. 1122–1127. IEEE, 2019.

[18] J. Fournet and A. Barrat. Contact patterns among high school students. *PLOS One*, 9(9), 2014.

[19] T. Fujiwara, J.-K. Chou, A. M. McCullough, C. Ranganath, and K.-L. Ma. A visual analytics system for brain functional connectivity comparison across individuals, groups, and time points. In *Proc. PacificVis*, pp. 250–259. IEEE, 2017.

[20] T. Fujiwara, J.-K. Chou, S. Shilpika, P. Xu, L. Ren, and K.-L. Ma. An incremental dimensionality reduction method for visualizing streaming multidimensional data. *IEEE Transactions on Visualization and Computer Graphics*, 26(1):418–428, 2020.

[21] T. Fujiwara, O.-H. Kwon, and K.-L. Ma. Supporting analysis of dimensionality reduction results with contrastive learning. *IEEE Transactions on Visualization and Computer Graphics*, 26(1):45–55, 2019.

[22] T. Fujiwara, J. K. Li, M. Mubarak, C. Ross, C. D. Carothers, R. B. Ross, and K.-L. Ma. A visual analytics system for optimizing the performance of large-scale networks in supercomputing systems. *Visual Informatics*, 2(1):98–110, 2018.

[23] H. Guo, S. Di, R. Gupta, T. Peterka, and F. Cappello. La VALSE: Scalable log visualization for fault characterization in supercomputers. In *Proc. EGPGV*, pp. 91–100. Eurographics, 2018.

[24] R. Guo, T. Fujiwara, Y. Li, K. M. Lima, S. Sen, N. K. Tran, and K.-L. Ma. Comparative visual analytics for assessing medical records with sequence embedding. *Visual Informatics*, 4(2):72–85, 2020.

[25] R. A. Harshman. Foundations of the PARAFAC procedure: Models and conditions for an “explanatory” multi-mode factor analysis. *UCLA Working Papers in Phonetics*, 16:1–84, 1970.

[26] H. Hassani and R. Mahmoudvand. Multivariate singular spectrum analysis. In *Singular Spectrum Analysis*, pp. 49–86. Springer, 2018.

[27] L. Huang, A. L. Shea, H. Qian, A. Masurkar, H. Deng, and D. Liu. Patient clustering improves efficiency of federated machine learning to predict mortality and hospital stay time using distributed electronic medical records. *Journal of Biomedical Informatics*, 99:103291, 2019.

[28] D. Jäckle, F. Fischer, T. Schreck, and D. A. Keim. Temporal MDS plots for analysis of multivariate data. *IEEE Transactions on Visualization and Computer Graphics*, 22(1):141–150, 2016.

[29] S. P. Kesavan, T. Fujiwara, J. K. Li, C. Ross, M. Mubarak, C. D. Carothers, R. B. Ross, and K.-L. Ma. A visual analytics framework for reviewing streaming performance data. In *Proc. PacificVis*, pp. 206–2015, 2020.

[30] H. A. Kiers. Hierarchical relations among three-way methods. *Psychometrika*, 56(3):449–470, 1991.

[31] H. A. Kiers. Towards a standardized notation and terminology in multiway analysis. *Journal of Chemometrics: A Journal of the Chemometrics Society*, 14(3):105–122, 2000.

[32] T. G. Kolda and B. W. Bader. Tensor decompositions and applications. *SIAM Review*, 51(3):455–500, 2009.

[33] C. Lee, Z. Luo, K. Y. Ngiam, M. Zhang, K. Zheng, G. Chen, B. C. Ooi, and W. L. J. Yip. Big healthcare data analytics: Challenges and applications. In *Handbook of Large-Scale Distributed Computing in Smart Healthcare*, pp. 11–41. Springer, 2017.

[34] J. A. Lee and M. Verleysen. Quality assessment of dimensionality reduction: Rank-based criteria. *Neurocomputing*, 72(7-9):1431–1443, 2009.

[35] D. Liu, P. Xu, and L. Ren. TPFlow: Progressive partition and multidimensional pattern extraction for large-scale spatio-temporal data analysis. *IEEE Transactions on Visualization and Computer Graphics*, 25(1):1–11, 2019.

[36] S. Liu, D. Maljovec, B. Wang, P.-T. Bremer, and V. Pascucci. Visualizing high-dimensional data: Advances in the past decade. *IEEE Transactions on Visualization and Computer Graphics*, 23(3):1249–1268, 2016.

[37] H. Lu, K. N. Plataniotis, and A. N. Venetsanopoulos. A survey of multi-linear subspace learning for tensor data. *Pattern Recognition*, 44(7):1540–1551, 2011.

[38] L. McInnes, J. Healy, and J. Melville. UMAP: Uniform manifold approximation and projection for dimension reduction. *arXiv:1802.03426*, 2018.

[39] H. Miyazaki, Y. Kusano, N. Shinjou, F. Shoji, M. Yokokawa, and T. Watanabe. Overview of the K computer system. *Fujitsu Scientific & Technical Journal*, 48(3):302–309, 2012.

[40] C. Muelder, B. Zhu, W. Chen, H. Zhang, and K.-L. Ma. Visual analysis of cloud computing performance using behavioral lines. *IEEE Transactions on Visualization and Computer Graphics*, 22(6):1694–1704, 2016.

[41] M. Newman. *Networks*. Oxford university press, 2018.

[42] L. G. Nonato and M. Aupetit. Multidimensional projection for visual analytics: Linking techniques with distortions, tasks, and layout enrichment. *IEEE Transactions on Visualization and Computer Graphics*, 25(8):2650–2673, 2019.

[43] P. E. Rauber, A. X. Falcão, and A. C. Telea. Visualizing time-dependent data using dynamic t-SNE. *Proc. EuroVis*, 2(5):73–77, 2016.

[44] R. A. Rossi, R. Zhou, and N. Ahmed. Deep inductive graph representation learning. *IEEE Transactions on Knowledge and Data Engineering*, 32(3):438–452, 2020.

[45] D. Sacha, L. Zhang, M. Sedlmair, J. A. Lee, J. Peltonen, D. Weiskopf, S. C. North, and D. A. Keim. Visual interaction with dimensionality reduction: A structured literature analysis. *IEEE Transactions on Visualization and Computer Graphics*, 23(1):241–250, 2017.

[46] F. Shilpika, B. Lusch, M. Emani, V. Vishwanath, M. E. Papka, and K.-L. Ma. MELA: A visual analytics tool for studying multifidelity hpc system logs. In *Proc. DAAC*, pp. 13–18. IEEE, 2019.

[47] Y. Sun, H. Song, A. J. Jara, and R. Bie. Internet of things and big data analytics for smart and connected communities. *IEEE Access*, 4:766–773, 2016.

[48] L. R. Tucker. Some mathematical notes on three-mode factor analysis. *Psychometrika*, 31(3):279–311, 1966.

[49] C. Turky, E. Kaya, S. Balcisoy, and H. Hauser. Designing progressive and

interactive analytics processes for high-dimensional data analysis. *IEEE Transactions on Visualization and Computer Graphics*, 23(1):131–140, 2017.

[50] US Environmental Protection Agency. Air quality system data mart. <https://www.epa.gov/airdata>, 2019. Accessed: 2020-4-21.

[51] S. van den Elzen, D. Holten, J. Blaas, and J. J. van Wijk. Reducing snapshots to points: A visual analytics approach to dynamic network exploration. *IEEE Transactions on Visualization and Computer Graphics*, 22(1):1–10, 2016.

[52] L. van der Maaten and G. Hinton. Visualizing data using t-SNE. *Journal of Machine Learning Research*, 9(Nov):2579–2605, 2008.

[53] L. van der Maaten, E. Postma, and J. van den Herik. Dimensionality reduction: A comparative review. *Journal of Machine Learning Research*, 10:66–71, 2009.

[54] T. von Landesberger, F. Brodkorb, P. Roskosch, N. Andrienko, G. Andrienko, and A. Kerren. MobilityGraphs: Visual analysis of mass mobility dynamics via spatio-temporal graphs and clustering. *IEEE Transactions on Visualization and Computer Graphics*, 22(1):11–20, 2016.

[55] J.-L. Wang, J.-M. Chiou, and H.-G. Müller. Functional data analysis. *Annual Review of Statistics and Its Application*, 3:257–295, 2016.

[56] Y. Wang and K.-L. Ma. Revealing the fog-of-war: A visualization-directed, uncertainty-aware approach for exploring high-dimensional data. In *Proc. IEEE BigData*, pp. 629–638, 2015.

[57] W. Wu, Y. Zheng, K. Chen, X. Wang, and N. Cao. A visual analytics approach for equipment condition monitoring in smart factories of process industry. In *Proc. PacificVis*, pp. 140–149. IEEE, 2018.

[58] P. Xu, H. Mei, L. Ren, and W. Chen. ViDX: Visual diagnostics of assembly line performance in smart factories. *IEEE Transactions on Visualization and Computer Graphics*, 23(1):291–300, 2017.

[59] F. Zhou, X. Lin, C. Liu, Y. Zhao, P. Xu, L. Ren, T. Xue, and L. Ren. A survey of visualization for smart manufacturing. *Journal of Visualization*, 22(2):419–435, 2019.